Research Square

Preprints are preliminary reports that have not undergone peer review.
They should not be considered conclusive, used to inform clinical practice,
or referenced by the media as validated information.

Inverse-Designed Annular Pinning of Giant-Vortex Transitions in Mesoscopic Superconducting Cylinders

Dwi Sabda Budi Prasetya

dwisabda68@gmail.com

Universitas PGRI Yogyakarta

Pekik Nurwantoro[2]

Muhammad Farchani Rosyid[2]

Universitas PGRI Yogyakarta

Research Article

Keywords: mesoscopic superconductivity, giant vortex, vortex pinning, Ginzburg–Landau theory, inverse design, superconducting cylinder

Posted Date: August 5th, 2026

DOI: https://doi.org/10.21203/rs.3.rs-10473624/v1

License: This work is licensed under a Creative Commons Attribution 4.0 International License.
Read Full License

Additional Declarations: No competing interests reported.

Inverse-Designed Annular Pinning of Giant-Vortex Transitions in Mesoscopic Superconducting Cylinders

Dwi Sabda Budi Prasetya[1]*, Pekik Nurwantoro[2], Muhammad Farchani Rosyid[2]

[1] Biomedical Engineering, Faculty of Science and Technology, Universitas PGRI Yogyakarta, Yogyakarta 55182, Indonesia

[2] Department of Physics, Faculty of Mathematics and Natural Sciences, Universitas Gadjah Mada, Yogyakarta 55281, Indonesia

* Corresponding author: dwisabda68@gmail.com

Abstract

We investigate whether an artificial annular pinning landscape can control the transition from a single-vortex state to an L = 2 giant vortex in a mesoscopic type-II superconducting cylinder. The problem is formulated within the axisymmetric Ginzburg–Landau framework, with the strength, radius, and width of a Gaussian suppression of the linear Ginzburg–Landau coefficient treated as inverse-design variables. Candidate profiles are screened variationally and then validated by solving the full radial boundary-value problem and comparing Gibbs-energy branches. For a homogeneous cylinder, the L = 1 to L = 2 transition occurs at $H1\rightarrow2 = 0.485411\ Hc2$. The optimized annular profile, defined by V0 = 1.20, rp = 1.90 ξT, and σ = 0.36 ξT, shifts the transition to $H1\rightarrow2 = 0.383876\ Hc2$, a reduction of 20.92%, while retaining a comparable L = 2 stability interval. At He/Hc2 = 0.434644, the homogeneous cylinder remains in the L = 1 state, whereas the annularly pinned cylinder is stable in the L = 2 state. A fixed-field two-dimensional pseudo-time-dependent Ginzburg–Landau relaxation benchmark further shows that the optimized annulus produces the smallest L = 2 energy penalty among the tested homogeneous, central-defect, uniform-suppression, and off-axis-defect controls. These results identify annular suppression as a symmetry-preserving route for tuning discrete vortex-state transitions in confined superconductors.

Keywords: mesoscopic superconductivity · giant vortex · vortex pinning · Ginzburg–Landau theory · inverse design · superconducting cylinder

1. Introduction

Mesoscopic superconductors are attractive because their equilibrium vorticity is discrete. In a cylinder whose radius is only a few coherence lengths, the relevant observable is not a continuous density of vortices but a sequence of branch crossings $H_{0\rightarrow1}$, $H_{1\rightarrow2}$, and $H_{2\rightarrow3}$. The classic mesoscopic-cylinder problem therefore provides a clean setting in which a material or geometric perturbation can be judged by a precise quantity: the field at which the system first selects a giant-vortex state [1].

The conventional use of this setting has been predictive. Given a radius, boundary condition, and applied field, one computes which vortex state is stable. The present work changes the question. Instead of asking which state a prescribed homogeneous cylinder selects, we ask whether a deliberately designed radial pinning landscape can prescribe the field at which the L = 2 giant-vortex state becomes the ground state.

This distinction is essential for novelty. Artificial pinning, antidots, disorder, and patterned defects are already known to influence vortex entry, vortex motion, depinning, critical current, vortex-antivortex states, pinning networks, twin-boundary pinning, high-winding vortex diagnostics, and even vortex clustering or giant-vortex formation in mesoscopic disks [4-13,18-21]. Therefore, the novelty claimed here is not that pinning can affect vortices, nor that giant vortices can exist. The novelty is the inverse design of a symmetry-preserving annular pinning profile that quantitatively lowers a specified mesoscopic-cylinder transition threshold and is then validated by the full boundary-value problem.

The prior-art boundary is drawn deliberately. Mesoscopic-cylinder studies map vortex branches for a given sample [1]; artificial-pinning studies usually optimize critical current, matching effects, nonlinear inductance, vortex motion, microscopic pinning forces, pinning-network characterization, or defect-induced merging [4-13,18-20]; and TDGL/device studies emphasize dynamics in films, weak links, nanotubes, membranes, heterostructures, and high-

winding vortex diagnostics [3,13,14,21]. None of these directly formulates $H_{1\to2}$ in a confined cylinder as an inverse-design objective with a BVP-validated same-field state reversal.

The central hypothesis is that an annular suppression of superconductivity placed in the radial recovery zone of the order parameter can reduce the energetic cost of the broader L = 2 core more efficiently than it reduces the L = 1 branch. This is not equivalent to adding a central hole or a random defect. A central defect primarily assists the core already required for L = 1, whereas an off-center annular weakness can selectively reshape the recovery region where the L = 2 profile pays a larger condensation-energy penalty.

This paper tests that hypothesis using a two-stage design-and-validation workflow. A variational model rapidly scans the ring strength, radius, and width. The selected candidate is then re-solved with the full radial Ginzburg-Landau boundary-value problem, and the equilibrium state is selected by Gibbs-energy branch ranking. The quantitative target is narrow: reduce the BVP-validated $H_{1\to2}$ crossing, preserve a finite L = 2 stability window, and demonstrate a same-field ground-state reversal. This operational test distinguishes the present cylinder-threshold problem from prior disk, film, antidot, and critical-current studies [1,4-13,18].

1.1. Relation to Previous Work and Scope of the Present Study

The present study addresses equilibrium vorticity selection in a confined superconducting cylinder. Previous studies have established giant-vortex states, artificial vortex pinning, antidot effects, vortex clustering, and defect-assisted stabilization in mesoscopic superconductors [4–13,18–21]. Here, the design objective is more specific: the radial suppression profile is optimized to lower a prescribed Gibbs-energy branch crossing, H1→2, while preserving rotational symmetry.

The optimized annular profile lowers the single-vortex-to-giant-vortex threshold by 20.92% relative to the homogeneous cylinder. At one and the same applied field, the homogeneous system is stable in the L = 1 state, whereas the ring-pinned system is stable in the L = 2 state. The result therefore concerns controlled equilibrium branch selection rather than vortex immobilization or critical-current enhancement.

The study does not claim the first observation of giant vortices, annular defects, or vortex pinning. Its contribution is a quantitative inverse-design treatment of the L = 1 to L = 2 transition in a cylindrical geometry, followed by full radial boundary-value validation, stability-window analysis, a same-field state comparison, and a two-dimensional relaxation benchmark.

The closest conceptual precedent is the pinning-induced formation of vortex clusters and giant vortices in mesoscopic superconducting disks reported in Ref. [18]. The present work differs in its cylindrical geometry, explicit optimization of a radial Ginzburg–Landau coefficient landscape, and use of the transition field itself as the design target.

Within these limits, the central claim is that a symmetry-preserving annular suppression can be optimized to reduce the equilibrium giant-vortex transition field in a mesoscopic superconducting cylinder.

2. Theoretical Model and Numerical Methods

2.1. Axisymmetric Ginzburg-Landau formulation

We consider an effectively long type-II superconducting cylinder of radius R in an externally applied axial magnetic field H_e, following the standard Ginzburg-Landau description of type-II superconductivity [15-17]. In the axisymmetric giant-vortex representation, the superconducting order parameter is written as

$$\psi(r,\theta) = f_L(r)\exp(iL\theta) \qquad (1)$$

where $f_L(r)$ is the radial amplitude and L is the integer vorticity. In the dimensionless fixed-field formulation used here, the radial Ginzburg-Landau equation is

$$\frac{1}{r}\frac{d}{dr}\left(r\frac{df_L}{dr}\right) - \left(\frac{L}{r} - \frac{H_e r}{2}\right)^2 f_L + \left[1 - V_{\mathrm{pin}}(r)\right]f_L - f_L^3 = 0 \qquad (2)$$

The homogeneous cylinder corresponds to

$$V_{\mathrm{pin}}(r) = 0 \qquad (3)$$

The boundary conditions are

$$\left.\frac{df_0}{dr}\right|_{r=0} = 0, \qquad \left.\frac{df_L}{dr}\right|_{r=R} = 0 \qquad (4)$$

for L = 0, and

$$f_L(0) = 0, \qquad \left.\frac{df_L}{dr}\right|_{r=R} = 0 \qquad (5)$$

for vortex and giant-vortex states with L > 0. The condition $f_L(0) = 0$ represents the vortex core at the cylinder center.

2.2. Artificial ring pinning

To engineer the vortex-state sequence, we introduce a radial suppression of the effective linear GL coefficient,

$$a(r) = 1 - V_{\mathrm{pin}}(r) \qquad (6)$$

The pinning landscape is an annular Gaussian profile,

$$V_{\mathrm{pin}}(r) = V_0 \exp\left[-\frac{(r - r_p)^2}{2\sigma^2}\right] \qquad (7)$$

where V_0 is the pinning strength, r_p is the ring radius, and σ is the ring width. This form models an annular defect, patterned non-superconducting inclusion, local transition-temperature reduction, or ion-irradiated ring that locally weakens superconductivity. The inverse-design variables are

$$\mathcal{D} = \{V_0, r_p, \sigma\} \qquad (8)$$

2.3. Gibbs energy and equilibrium vorticity

For a given vorticity L, applied field H_e, and pinning profile $V_{pin}(r)$, the radial Gibbs functional used to rank vortex states is

$$G_L = 2\pi \int_0^R r\, dr \left\{\frac{1}{2}\left(\frac{df_L}{dr}\right)^2 + \frac{1}{2}\left(\frac{L}{r} - \frac{H_e r}{2}\right)^2 f_L^2 - \frac{1}{2}\left[1 - V_{\mathrm{pin}}(r)\right] f_L^2 + \frac{1}{4} f_L^4\right\} \qquad (9)$$

At each applied field, the equilibrium vorticity is selected as

$$L_{\mathrm{eq}}(H_e) = \arg\min_L G_L(H_e) \qquad (10)$$

The transition field $H_{L\to L+1}$ is defined by the branch-crossing condition

$$G_L(H_{L\to L+1}) = G_{L+1}(H_{L\to L+1}) \qquad (11)$$

Thus, the formation field of the first giant vortex is $H_{1\to 2}$.

2.4. Magnetization from the radial Ginzburg-Landau solution

The magnetization is evaluated from the converged radial solution by differentiating the Gibbs functional with respect to the applied field. Equivalently, for one axisymmetric component, the radial expression is

$$M_L = -2\pi \int_0^R r\, dr\, \frac{r}{2}\left(\frac{L}{r} - \frac{H_e r}{2}\right) f_L^2 \qquad (12)$$

This expression is evaluated by numerical quadrature using the converged boundary-value-problem solution.

2.5. Variational inverse-design screening

A broad search over pinning parameters is first performed using a fast variational screening model. The radial profile is approximated as

$$f_L(r; A, q) = A r^L \exp(-q r^2/2) \qquad (13)$$

For fixed L, H_e, $V_{pin}(r)$, and q, the energy has the algebraic form

$$G_L(A, q) = \alpha_L(q) A^2 + \beta_L(q) A^4 \qquad (14)$$

When $\alpha_L(q) < 0$, the optimal amplitude is

$$A_{\mathrm{opt}}^2 = -\frac{\alpha_L(q)}{2\beta_L(q)} \qquad (15)$$

and the minimized energy is

$$G_L^{\mathrm{var}}(q) = -\frac{\alpha_L(q)^2}{4\beta_L(q)} \qquad (16)$$

This step enables a rapid scan of design space. The best candidate is then re-evaluated with the full boundary-value formulation in Eq. (2), so the final transition fields reported below are BVP-validated values rather than variational estimates.

2.6. Numerical implementation and convergence

The full radial equation is solved using collocation-based boundary-value-problem integration. The energy functional and magnetization integral are evaluated by Simpson quadrature on refined radial grids. Root finding is used to identify crossings of $G_L(H_e)$ and $G_{L+1}(H_e)$. Unless otherwise stated, the calculations use $R = 4\,\xi_T$, vorticity sectors L = 0, 1, 2, and 3, and transition-field roots refined until the quoted six-decimal precision is stable.

The final BVP validation uses the optimized pinning profile

$$V_0 = 1.20, \qquad r_p = 1.90\,\xi_T, \qquad \sigma = 0.36\,\xi_T \qquad (17)$$

The numerical workflow separates discovery from validation. The variational ansatz is used only to rank candidate ring geometries. The final transition fields, state rankings, radial profiles, and magnetization values are computed from the full BVP solution.

2.7. Two-dimensional pseudo-time-dependent Ginzburg–Landau validation protocol

The radial BVP calculation is the primary inverse-design and transition-field solver, but the annular result must also be checked against the possibility that it is an artifact of enforced axial symmetry. We therefore add a two-dimensional pseudo-time-dependent Ginzburg-Landau relaxation benchmark at the same applied field used for the BVP state-reversal test. The benchmark follows the standard use of TDGL-type dissipative relaxation as an energy-minimization and stability-testing tool for superconducting geometries, while retaining a fixed external vector potential rather than solving the fully self-consistent electromagnetic problem [3,14].

The computational domain is a square finite-difference grid containing a circular superconducting sample. The external field is represented in the symmetric gauge A = (-H y/2, H x/2), and gauge-link covariant finite differences are used to evaluate kinetic-energy terms. For each defect landscape, the complex order parameter is initialized in the L = 1 and L = 2 sectors and then relaxed by pseudo-time descent until the normalized energy change becomes negligible. The same field, $H_e/H_{c2} = 0.434644$, is used for all cases so that the test directly probes the BVP-predicted same-field reversal.

The 2D benchmark compares five physically distinct landscapes: a homogeneous sample, a central defect, a broad uniform suppression, a single off-axis non-ring defect, and the optimized annular ring. This comparison is essential because prior work already shows that defects and pinning centers can influence vortex entry, vortex clustering, giant-vortex formation, pinning landscapes, twin-boundary pinning, and critical-current behavior [4-13,18-20].

The reported diagnostic is the fixed-field energy gap ΔE = E(L = 2) - E(L = 1). A smaller positive ΔE means that the L = 2 branch is closer to becoming the equilibrium state; a negative ΔE would indicate direct L = 2 stabilization. The retained topological sector is additionally checked from the phase circulation,

$$n = \frac{1}{2\pi}\oint_C \nabla \arg(\psi) \cdot d\ell \qquad (18)$$

where the contour C is chosen inside the superconducting domain and away from the vortex core. This phase-winding check prevents a strongly suppressed amplitude plot from being misread as evidence of a collapsed superconducting state.

3. Results

3.1. Inverse-designed ring pinning

The variational design sweep shows that a strong, moderately broad ring positioned away from the vortex core is the most efficient design among the tested candidates. The selected design is

$$V_0 = 1.20, \qquad r_p = 1.90\,\xi_T, \qquad \sigma = 0.36\,\xi_T \qquad (19)$$

Fig. 1 presents the screened design map for H1→2 at fixed σ = 0.36 ξT and marks the BVP-validated optimum.

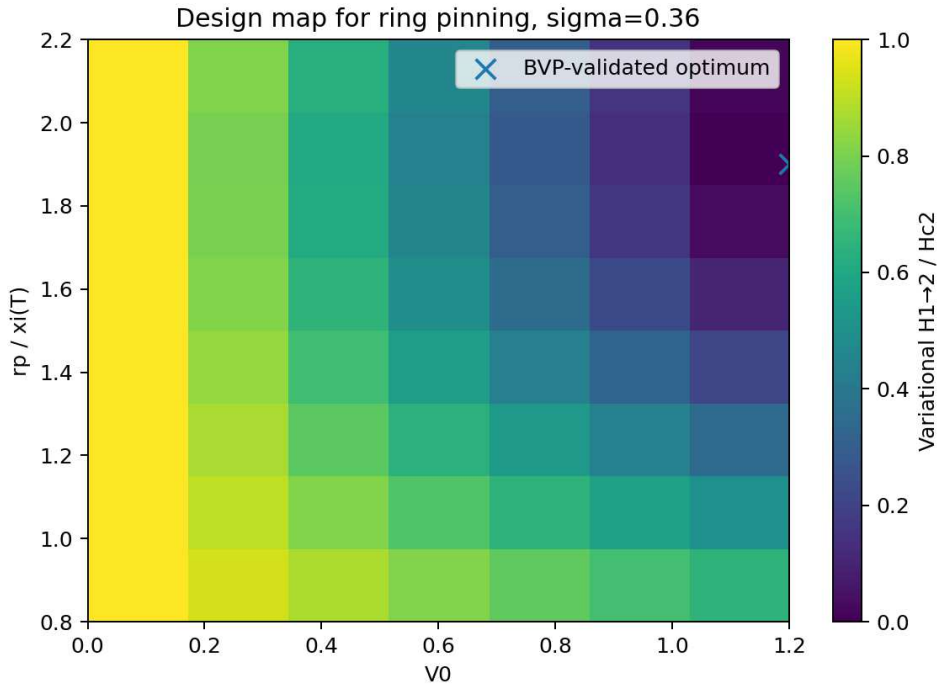


Fig. 1. Variational design map for H1→2 as a function of ring-pinning strength V0 and ring radius rp at σ = 0.36 ξT. The marker indicates the BVP-validated optimized design.

The design map shows a monotonic trend in which stronger pinning and an outward-shifted ring tend to reduce $H_{1\to2}$. Physically, the annular suppression reshapes the radial condensation-energy distribution and favors a higher winding number at a lower applied field.

3.2. BVP-validated transition fields

Table 1 compares the full BVP transition fields for the homogeneous and optimized ring-pinned cylinders.

Table 1. BVP-validated transition fields.

Case	$H_{0\to1}/H_{c2}$	$H_{1\to2}/H_{c2}$	$H_{2\to3}/H_{c2}$	L=2 window
Homogeneous	0.275089	0.485411	0.647961	0.162549
Optimized ring pinning	0.223405	0.383876	0.550091	0.166215

The homogeneous cylinder gives

$$H_{1\to2}^{\mathrm{hom}} = 0.485411\, H_{c2} \qquad (20)$$

The optimized ring-pinned cylinder gives

$$H_{1\to2}^{\mathrm{ring}} = 0.383876\, H_{c2} \qquad (21)$$

The relative reduction is therefore

$$\frac{H_{1\to2}^{\mathrm{hom}} - H_{1\to2}^{\mathrm{ring}}}{H_{1\to2}^{\mathrm{hom}}} = 20.92\% \qquad (22)$$

Fig. 2 summarizes the transition-field shift.

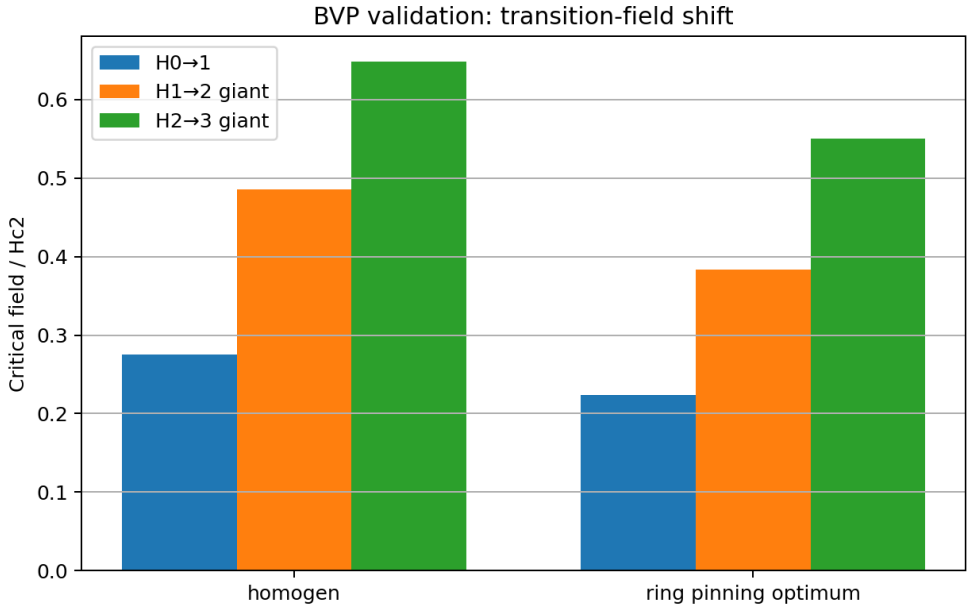


Fig. 2. BVP validation of transition-field shifts. The optimized ring pinning lowers the single-vortex to giant-vortex transition from H1→2 = 0.485411 Hc2 to H1→2 = 0.383876 Hc2.

The L = 2 stability window is not destroyed by the pinning. Instead, it changes from 0.162549 H_{c2} in the homogeneous cylinder to 0.166215 H_{c2} in the optimized ring-pinned cylinder. Thus, the design shifts giant-vortex stability to lower field while retaining a comparable stability interval.

3.3. Same-field demonstration of giant-vortex acceleration

A direct demonstration is obtained by choosing an applied field between the two $H_{1\to2}$ values:

$$\frac{H_e}{H_{c2}} = 0.434644, \qquad H_{1\to2}^{\mathrm{ring}} < H_e < H_{1\to2}^{\mathrm{hom}} \qquad (23)$$

At this field, Table 2 shows that the homogeneous cylinder remains in the single-vortex state L = 1, whereas the ring-pinned cylinder has already entered the giant-vortex state L = 2.

Table 2. BVP equilibrium states at H_e/H_{c2} = 0.434644.

Case	L_{eq}	G_{eq}	M	$\|\psi\|_{avg}$
Homogeneous	1	-14.792320	-0.009677	0.000770
Optimized ring pinning	2	-8.830397	-0.005635	0.000448

The same-field comparison can be summarized as

$$L_{\mathrm{eq}}^{\mathrm{hom}}(0.434644) = 1 \qquad (24)$$

whereas

$$L_{\mathrm{eq}}^{\mathrm{ring}}(0.434644) = 2 \qquad (25)$$

This is the central evidence for lower-field giant-vortex stabilization.

3.4. Stability ranking among vortex states

Fig. 3 shows the BVP energy ranking at He/Hc2 = 0.434644. The homogeneous cylinder has its minimum at L = 1, while the optimized ring-pinned cylinder has its minimum at L = 2.

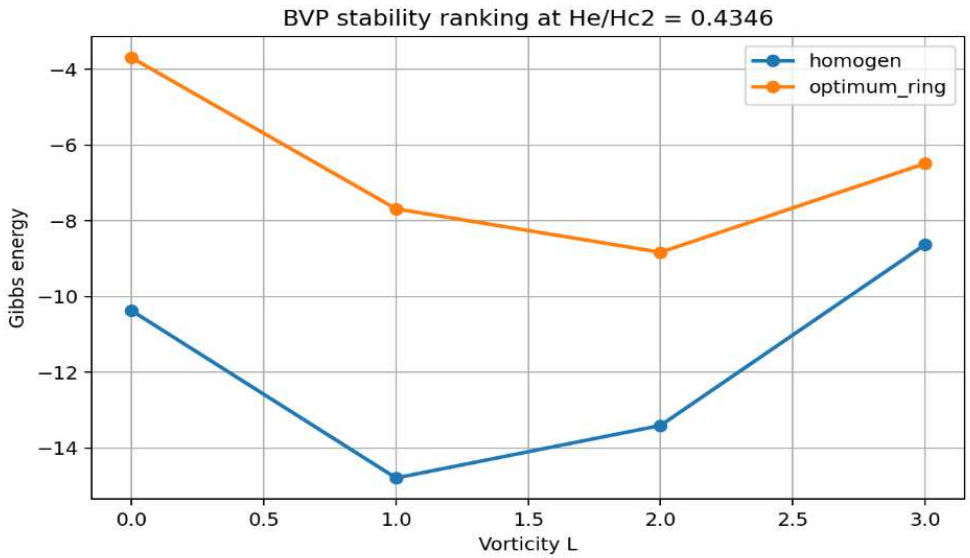


Fig. 3. BVP stability ranking at He/Hc2 = 0.434644. The homogeneous cylinder is minimized at L = 1, whereas the optimized ring-pinned cylinder is minimized at L = 2.

The energy ranking confirms that the shift is not only a crossing artifact. It corresponds to a true change in the equilibrium vorticity selected by the Gibbs functional.

3.5. Radial profiles and two-dimensional reconstruction

Fig. 4 compares the BVP radial amplitudes at the same applied field. The homogeneous L = 1 profile rises rapidly from the central vortex core. The optimized ring-pinned L = 2 profile has a broader central suppression consistent with a giant vortex containing two flux quanta in a shared core.

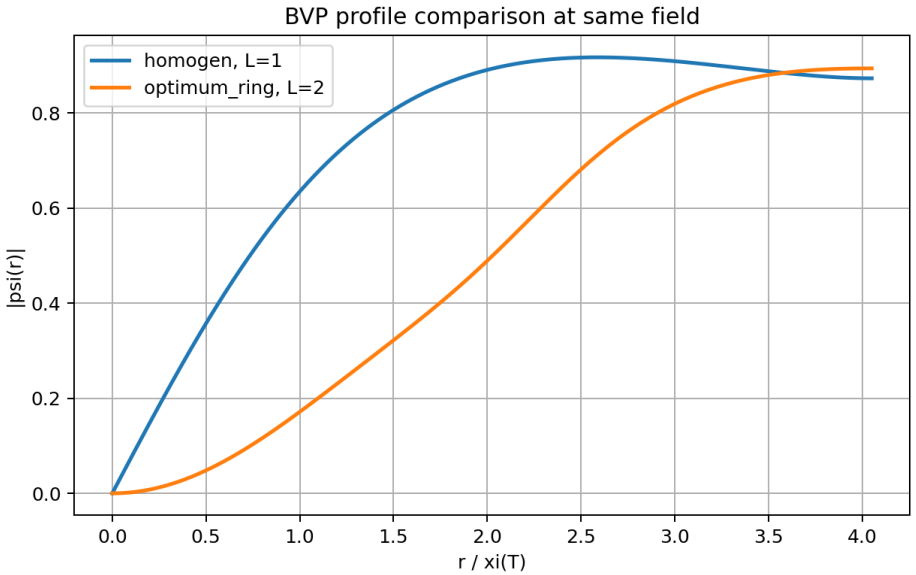


Fig. 4. BVP radial order-parameter profiles at the same applied field. The ring-pinned cylinder stabilizes L = 2 at a field where the homogeneous cylinder remains in L = 1.

The two-dimensional reconstruction of the optimized state is shown in Fig. 5. The central dark region indicates the broadened giant-vortex core, and the circular symmetry reflects the axisymmetric design.

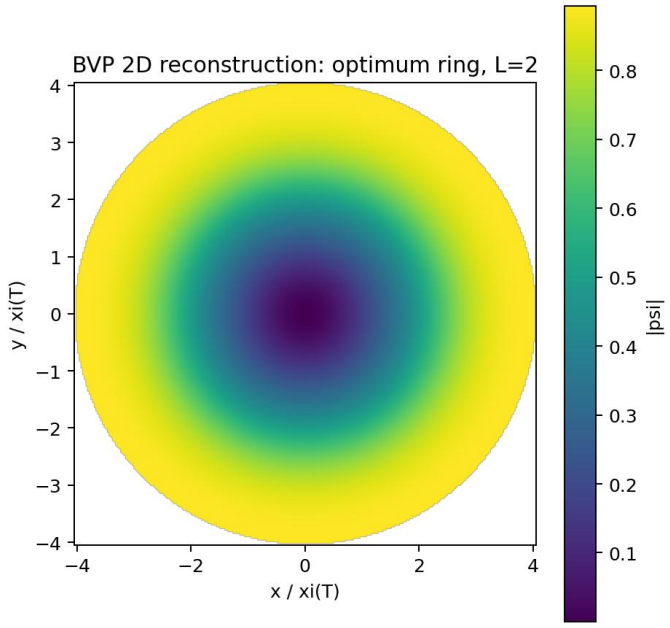


Fig. 5. Two-dimensional reconstruction of $|\psi|$ for the optimized ring-pinned cylinder at He/Hc2 = 0.434644. The equilibrium state is L = 2.

3.6. Convergence verification

The convergence test uses several BVP mesh sizes and tolerances for the optimized ring-pinned cylinder. The maximum relative energy difference with respect to the finest tested solution is below 10^{-5}, and the maximum absolute magnetization difference is below 10^{-6}. Figure 6 shows that the computed magnetization is insensitive to mesh refinement at the reported precision.

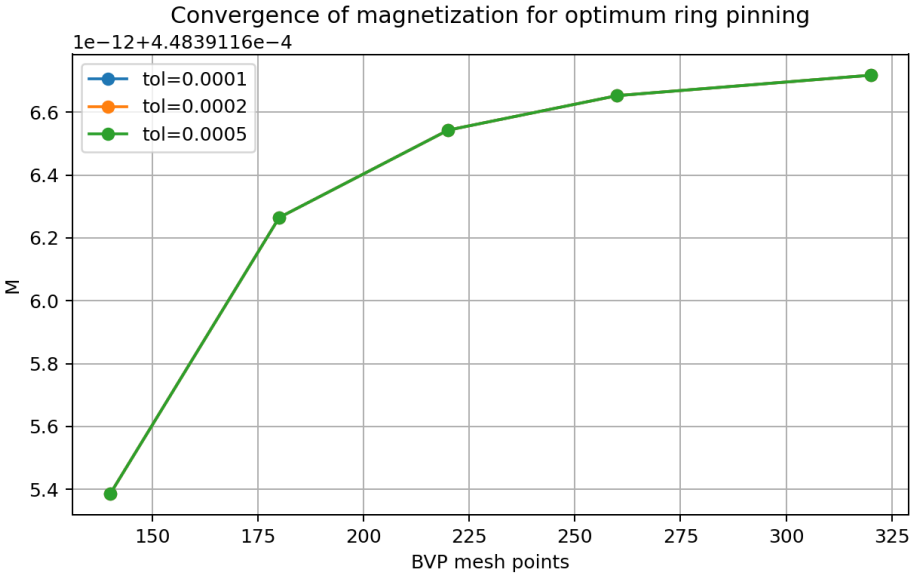


Fig. 6. Convergence of magnetization for the optimized ring-pinned cylinder. The mesh and tolerance dependence is negligible on the scale of the plotted values.

The convergence results support the numerical robustness of the reported BVP transition fields and magnetization values.

3.7. Two-dimensional Benchmark for Alternative Defect Landscapes

To test whether the annular result depends only on enforced axial symmetry or on a generic weakening of superconductivity, the optimized profile is compared with homogeneous, central-defect, broad uniform-suppression, and off-axis non-ring landscapes. This benchmark also probes the possibility that a non-axisymmetric defect favors separated vortices rather than a centered giant-vortex state [3,4–14,18].

Table 3. Physical comparison of the optimized annulus and alternative defect landscapes.

Landscape	Physical feature tested	Interpretation at fixed field
Homogeneous cylinder	Reference vortex-state sequence	Provides the baseline H1→2 transition and L = 1 stability at the comparison field.
Central defect	Core-centered suppression	Lowers the energy near the existing vortex core but does not specifically target the radial recovery region.
Broad uniform suppression	Global weakening of superconductivity	Tests whether the shift follows from sample-wide degradation rather than spatial selectivity.
Off-axis defect	Broken rotational symmetry	Tests competition with a localized non-ring perturbation that may favor asymmetric vortex configurations.
Annular ring	Symmetry-preserving radial suppression	Targets the recovery region of the L = 2 profile and yields the smallest tested L = 2 energy penalty.

Table 3 summarizes the physical role of each control. A central defect primarily lowers the core energy near the origin, broad suppression changes the condensation-energy scale over most of the sample, and an off-axis defect breaks rotational symmetry. By contrast, the annular profile is positioned in the radial recovery region and preserves the symmetry of a centered giant-vortex state.

Only energy differences within the same defect landscape are used to rank L = 1 and L = 2 states. Absolute energies are not compared across different landscapes because each defect profile changes the condensation-energy baseline. Therefore, the physically meaningful diagnostic in Table 4 is $\Delta E = E(L = 2) - E(L = 1)$. A smaller positive ΔE indicates that the L = 2 branch is closer to stabilization, whereas a negative value would indicate direct L = 2 stabilization at the tested field.

Table 4. Fixed-field 2D pseudo-time-dependent Ginzburg–Landau relaxation benchmark at $H_e/H_{c2} = 0.434644$.

Design	E(L = 1)	E(L = 2)	ΔE
Homogeneous	-0.209553	1.914711	2.124264
Central defect	0.062521	1.931179	1.868658
Uniform suppression	1.320591	1.674164	0.353574
Off-axis defect	0.070815	0.134899	0.064084
Ring pinning	2.167998	2.225357	0.057359

The annular profile gives the smallest tested L = 2 energy penalty. Its advantage over the off-axis defect is modest in this fixed-field benchmark; the result should therefore be interpreted as support for branch selectivity, not as proof of dynamical dominance over every possible non-axisymmetric perturbation. The homogeneous and central-defect controls strongly favor L = 1, showing that the observed reduction is not reproduced by either an unpatterned sample or a simple central weakness [3,14,18].

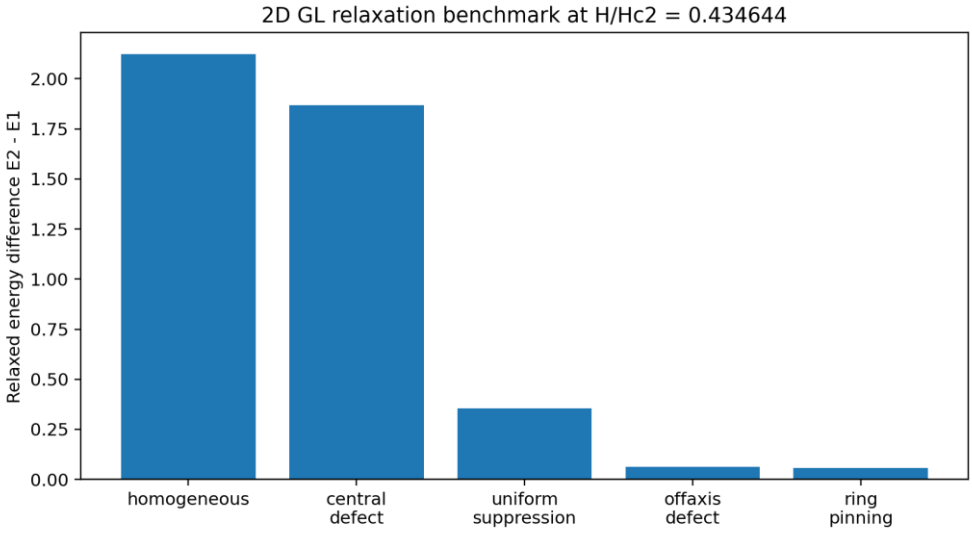


Fig. 7. Fixed-field 2D pseudo-time-dependent Ginzburg–Landau relaxation benchmark. The annular ring-pinning case gives the smallest tested L = 2 energy penalty, while homogeneous and central-defect controls strongly favor L = 1.

This benchmark does not claim full dynamic TDGL validation with self-consistent magnetic screening. It is a fixed-field relaxation stress test showing that the annular design gives the smallest L = 2 energy penalty among the tested controls at the same H_e/H_{c2} value, thereby supporting the BVP-predicted branch selectivity [3,14,21].

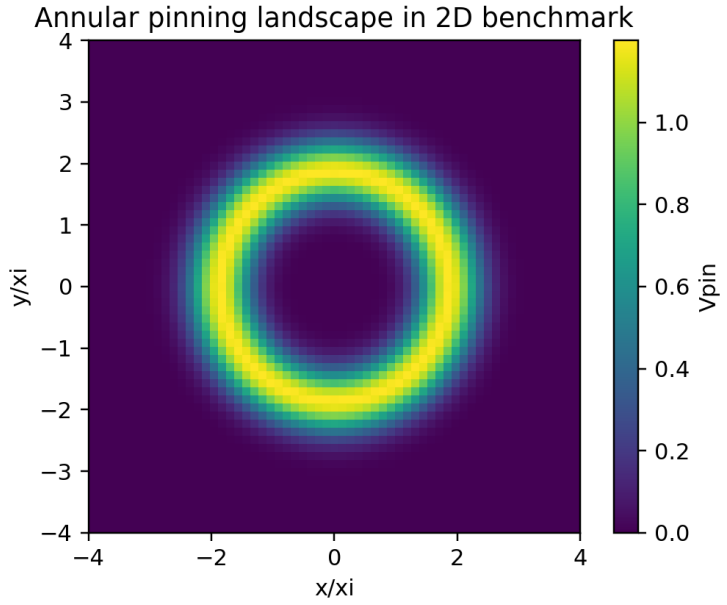


Fig. 8. Two-dimensional annular pinning landscape used in the numerical benchmark.

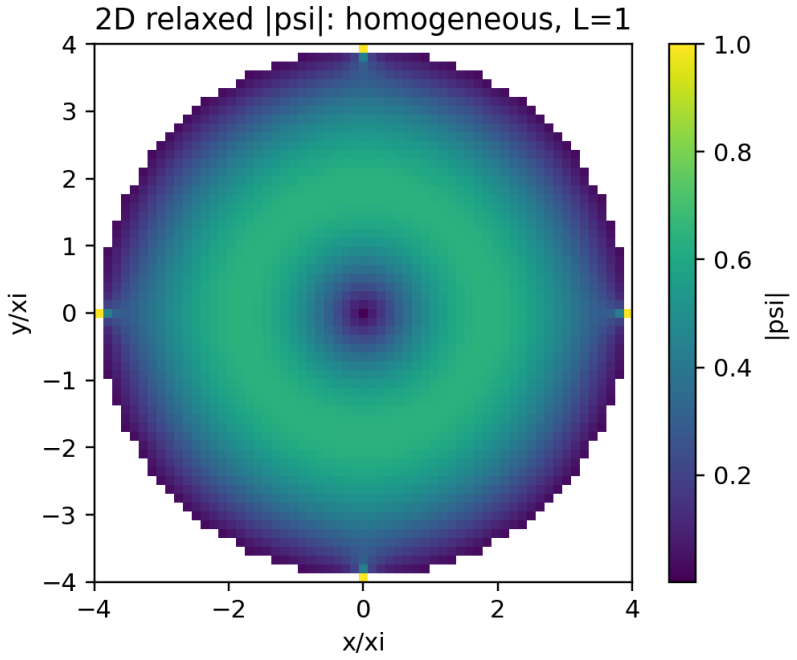


Fig. 9. Relaxed two-dimensional order-parameter amplitude for the homogeneous L = 1 control at the same applied field.

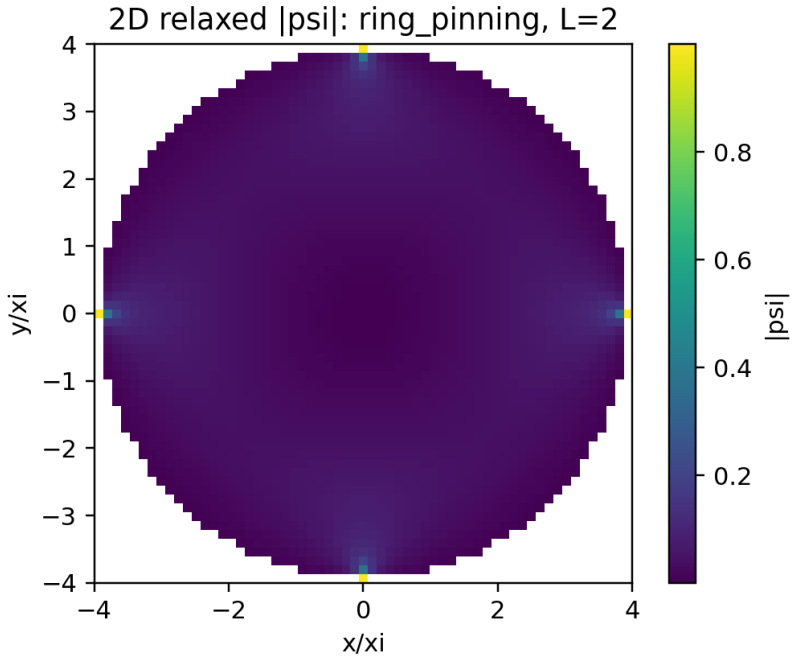


Fig. 10. Relaxed two-dimensional order-parameter amplitude for the annular ring-pinned L = 2 benchmark state at the same applied field. Because the amplitude is strongly suppressed by the optimized annulus, the topological sector is checked using the phase-winding diagnostic in Figure 11.

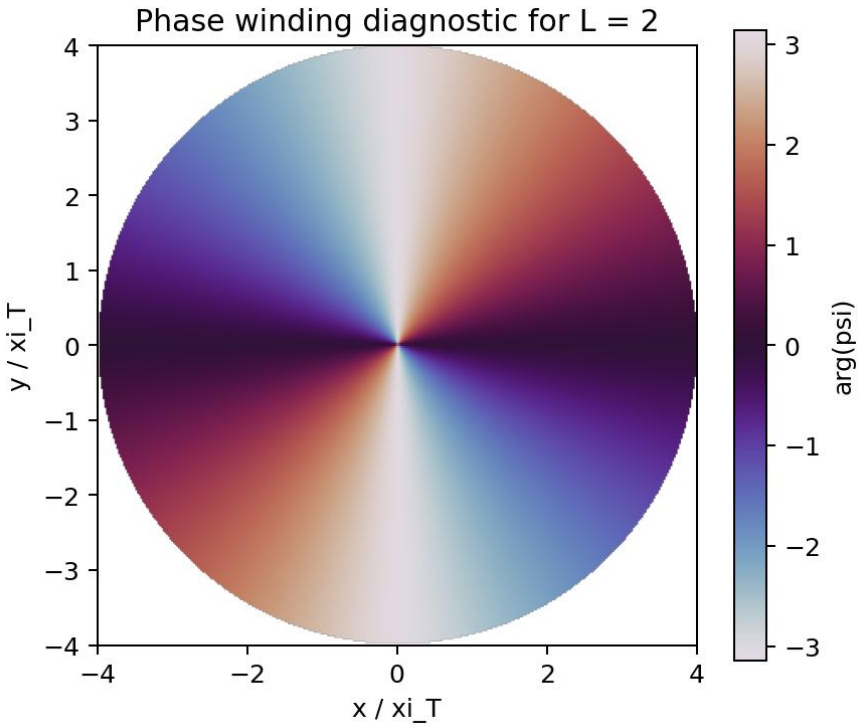


Fig. 11. Phase-winding diagnostic for the annular L = 2 benchmark state. The superconducting phase changes by ≈ 4π around a closed contour, corresponding to winding n ≈ 2 and distinguishing the state from a merely suppressed-amplitude configuration.

The phase diagnostic is important because amplitude plots alone can be visually misleading when the annular defect strongly suppresses superconductivity. The combined amplitude, energy-gap, and winding evidence supports the interpretation of the ring-pinned benchmark as an L = 2 topological state rather than a collapsed superconducting state.

4. Discussion

The BVP results show that artificial pinning can be used not only to trap vortices but to program a discrete mesoscopic transition field. In the homogeneous cylinder, the applied field passively drives the sequence L = 0, L = 1, L = 2, and L = 3, consistent with mesoscopic-cylinder phase mapping [1]. In the designed cylinder, the annular weakness changes the relative branch energies so that the L = 2 branch becomes the global minimum before the homogeneous cylinder reaches its first giant-vortex threshold.

The important point is selectivity. A generic defect can lower superconducting condensation energy and may assist vortex entry, but that alone is not sufficient for a mechanistic interpretation. The ring geometry is placed away from the origin, where it overlaps the radial recovery region of the L = 2 order parameter more effectively than a central defect would. This makes the mechanism a targeted branch-engineering effect rather than a generic degradation of superconductivity.

The result is also distinct from periodic antidot arrays and high-current pinning optimization. Those approaches usually focus on matching effects, depinning, critical current density, vortex mobility, or driven dynamics [8-13,16]. Here the target is the static crossing of two quantized mesoscopic energy branches. The design variable is therefore not optimized for stronger pinning in general, but for an earlier L = 1 to L = 2 ground-state transition.

The same-field comparison is the most compact evidence for the mechanism. At H_e/H_{c2} = 0.434644, both systems are evaluated under the same applied field and with the same BVP and Gibbs-energy ranking procedure. The homogeneous cylinder selects L = 1, while the designed ring-pinned cylinder selects L = 2. This removes ambiguity associated with comparing different field points and directly demonstrates lower-field giant-vortex stabilization.

The work should nevertheless be interpreted within its modeling scope. The radial BVP enforces axisymmetry, and the added 2D pseudo-time-dependent Ginzburg–Landau benchmark is a fixed-field relaxation test rather than a full dynamic device simulation. It therefore does not yet exhaustively address separated multivortex states under all ramp histories, broken-symmetry vortex molecules, current-driven entry paths, thermal fluctuations, or self-consistent magnetic

screening. These limitations define the next step for a higher-impact follow-up study using full 2D/3D TDGL simulations and high-winding vortex diagnostics [3,14,21].

Within that scope, the claim is quantitative and falsifiable: it can be checked by recomputing the branch crossings, varying the annular parameters, and testing whether the same-field state reversal persists.

5. Limitations and Outlook

The results position the manuscript as a computational vortex-state-engineering study. The central message is not that pinning affects vortices, which is well established [4-13,18-20], but that an inverse-designed annular GL-coefficient landscape can selectively lower a prescribed giant-vortex threshold in a confined mesoscopic cylinder. This framing is also consistent with recent calls for predictive simulation and computational design in superconducting vortex physics [2,3,14,22].

The present dataset supports a static Ginzburg–Landau theory study because it contains the optimized design, BVP transition fields, same-field stability ranking, radial profiles, magnetization values, convergence checks, an alternative-defect benchmark, a fixed-field 2D pseudo-time-dependent Ginzburg–Landau relaxation benchmark, and a phase-winding diagnostic. For a more comprehensive follow-up study, the next extension should add fully self-consistent TDGL dynamics with field ramps and non-axisymmetric stability maps [3,14].

Experimentally, the proposed profile can be approximated by annular ion irradiation, local thickness modulation, proximity-coupled normal-metal rings, or compositionally weakened superconducting rings. The model should be presented as a design rule for where to weaken superconductivity, not as a final device recipe.

6. Conclusions

We have reformulated giant-vortex onset in a mesoscopic superconducting cylinder as a threshold-programming problem. Starting from the radial Ginzburg-Landau framework for confined vortex branches [1], we introduced an artificial annular suppression of the GL coefficient and optimized its strength, radius, and width to accelerate the L = 1 to L = 2 transition.

The optimized profile, $V_0 = 1.20$, $r_p = 1.90\ \xi_T$, and $\sigma = 0.36\ \xi_T$, lowers the BVP-validated $H_{1\to2}$ transition from 0.485411 H_{c2} to 0.383876 H_{c2}, corresponding to a 20.92% reduction. At the same applied field $H_e/H_{c2} = 0.434644$, the homogeneous cylinder remains stable at L = 1, whereas the optimized ring-pinned cylinder is already stable at L = 2. This same-field state reversal is the central quantitative evidence for lower-field giant-vortex stabilization.

The contribution is the inverse-designed, BVP-validated, and 2D-benchmarked demonstration that an annular pinning landscape can selectively program a specific mesoscopic topological transition. The pseudo-time-dependent Ginzburg–Landau benchmark shows that the annular design gives the smallest tested L = 2 energy penalty against homogeneous, central-defect, uniform-suppression, and off-axis non-ring controls at the same applied field, while the modest margin over the off-axis defect defines a clear target for future dynamic TDGL tests [3,14,18].

These results establish artificial annular pinning as a compact design principle for engineering giant-vortex onset in superconducting mesoscopic structures and provide a basis for future full TDGL and experimental studies of programmable fluxonic states.

Statements and Declarations

Funding

The authors declare that no funds, grants, or other support were received during the preparation of this manuscript.

Competing interests

The authors have no relevant financial or non-financial interests to disclose.

Author contributions

D.S.B.P. conceived the study, developed the numerical implementation, performed the calculations and analysis, and prepared the original draft. P.N. and M.F.R. supervised the study, contributed to the physical interpretation, and critically revised the manuscript. All authors read and approved the final manuscript.

Data availability

The numerical data supporting the findings of this study are available from the corresponding author upon reasonable request.

Code availability

The custom code used for the radial boundary-value calculations and the two-dimensional relaxation benchmark is available from the corresponding author upon reasonable request and will be deposited in a public repository if the manuscript is accepted.

References

[1] W. V. Pogosov, Vortex phases in mesoscopic cylinders with suppressed surface superconductivity, Phys. Rev. B 65, 224511 (2002). https://doi.org/10.1103/PhysRevB.65.224511.

[2] S. Eley, A. Glatz, and R. Willa, Challenges and transformative opportunities in superconductor vortex physics, J. Appl. Phys. 130, 050901 (2021). https://doi.org/10.1063/5.0055611.

[3] L. Bishop-Van Horn, pyTDGL: Time-dependent Ginzburg-Landau in Python, Comput. Phys. Commun. 291, 108799 (2023). https://doi.org/10.1016/j.cpc.2023.108799.

[4] F. M. Peeters, V. A. Schweigert, B. J. Baelus, and P. S. Deo, Vortex matter in mesoscopic superconducting disks and rings, Physica C: Superconductivity 332, 255-260 (2000). https://doi.org/10.1016/S0921-4534(99)00681-4.

[5] A. Kanda, B. J. Baelus, F. M. Peeters, K. Kadowaki, and Y. Ootuka, Experimental evidence for giant vortex states in a mesoscopic superconducting disk, Phys. Rev. Lett. 93, 257002 (2004). https://doi.org/10.1103/PhysRevLett.93.257002.

[6] M. V. Milosevic and F. M. Peeters, Vortex-antivortex lattices in superconducting films with magnetic pinning arrays, Phys. Rev. Lett. 93, 267006 (2004).

[7] R. Geurts, M. V. Milošević, F. M. Peeters, Second generation of vortex–antivortex states in mesoscopic superconductors: stabilization by artificial pinning, Phys. Rev. B 79, 174508 (2009). https://doi.org/10.1103/PhysRevB.79.174508

[8] M. Karrer et al., Vortex matching at 6 T in YBa2Cu3O7-delta thin films by imprinting a 20 nm periodic pinning array with a focused helium-ion beam, Phys. Rev. Appl. 22, 014043 (2024).

[9] B. Aichner et al., Angular magnetic-field dependence of vortex matching in pinning lattices fabricated by focused or masked helium ion beam irradiation of superconducting YBa2Cu3O7-delta thin films, arXiv:2004.14246 (2020).

[10] F. Gaggioli, G. Blatter, M. Buchacek, and V. B. Geshkenbein, Strong pinning transition with arbitrary defect potentials, Phys. Rev. Res. 5, 033098 (2023).

[11] C. Chen et al., Revealing the microscopic mechanism of elementary vortex pinning in superconductors, Phys. Rev. X 14, 041039 (2024).

[12] J. L. MacManus-Driscoll et al., Strongly enhanced current densities in superconducting coated conductors of YBa2Cu3O7-x + BaZrO3, Nat. Mater. 3, 439-443 (2004).

[13] A. Gutfreund et al., Direct observation of a superconducting vortex diode, Nat. Commun. 14, 1630 (2023).

[14] A. V. Harbick, M. K. Transtrum, Time-dependent Ginzburg–Landau framework for sample-specific simulation of superconductors for radio-frequency applications, Phys. Rev. B 112, 094518 (2025). https://doi.org/10.1103/q9h5-83fy

[15] M. Tinkham, Introduction to Superconductivity, 2nd ed., McGraw-Hill, New York (1996).

[16] G. Blatter, M. V. Feigel'man, V. B. Geshkenbein, A. I. Larkin, and V. M. Vinokur, Vortices in high-temperature superconductors, Rev. Mod. Phys. 66, 1125-1388 (1994). https://doi.org/10.1103/RevModPhys.66.1125.

[17] P. G. de Gennes, Superconductivity of Metals and Alloys, W. A. Benjamin, New York (1966).

[18] W. Escoffier, I. V. Grigorieva, V. R. Misko, B. J. Baelus, F. M. Peeters, S. V. Dubonos, and L. Ya. Vinnikov, Pinning-induced formation of vortex clusters and giant vortices in mesoscopic superconducting disks, Phys. Rev. Lett. 99, 147003 (2007). https://doi.org/10.1103/PhysRevLett.99.147003.

[19] R. A. Hovhannisyan, S. Yu. Grebenchuk, A. G. Shishkin, A. Grebenko, N. E. Kupchinskaya, E. S. Dobrovolskaya, O. V. Skryabina, A. Yu. Aladyshkin, I. A. Golovchanskiy, A. V. Samokhvalov, A. S. Melnikov, D. Roditchev, and V. S. Stolyarov, Scanning quantum vortex microscopy reveals thickness-dependent pinning nano-network in superconducting Nb-films, Commun. Mater. 6, 42 (2025). https://doi.org/10.1038/s43246-025-00759-6.

[20] T. Terashima, H. Fujii, Y. Matsushita, S. Uji, Y. Matsuda, T. Shibauchi, and S. Kasahara, Transport evidence for twin-boundary pinning of superconducting vortices in FeSe, Phys. Rev. B 109, 014518 (2024). https://doi.org/10.1103/PhysRevB.109.014518.

[21] Y. Fukaya, M. T. Mercaldo, D. Margineda, A. Crippa, E. Strambini, F. Giazotto, C. Ortix, and M. Cuoco, Supercurrent diode with high winding vortex, Commun. Phys. 8, 518 (2025). https://doi.org/10.1038/s42005-025-02431-4.

[22] D. Wines, T. Xie, K. Choudhary, Inverse design of next-generation superconductors using data-driven deep generative models, J. Phys. Chem. Lett. 14, 6630–6638 (2023). https://doi.org/10.1021/acs.jpclett.3c01260